Research Article Vol. 33, No. 21 / 20 Oct 2025 / Optics Express 44378
Optics EXPRESS

Low-cost refractive index sensor based on a fiber Mach-Zehnder interferometer fabricated by chemical etching method

YIJIAN HUANG,[1,2,3] YING WANG,[1,3,*] GAIXIA XU,[2] CHANGRUI LIAO,[1,3] AND YIPING WANG[1,3]

[1]*Key Laboratory of Optoelectronic Devices and Systems of Ministry of Education/Guangdong Province, Shenzhen Key Laboratory of Photonic Devices and Sensing Systems for Internet of Things, State Key Laboratory of Radio Frequency Heterogeneous Integration, College of Physics and Optoelectronic Engineering, Shenzhen University, Shenzhen 518060, China*
[2]*Guangdong Key Laboratory for Biomedical Measurements and Ultrasound Imaging, National-Regional Key Technology Engineering Laboratory for Medical Ultrasound, School of Biomedical Engineering, Shenzhen University Medical School, Shenzhen 518060, China*
[3]*Shenzhen Key Laboratory of Ultrafast Laser Micro/Nano Manufacturing, Guangdong and Hong Kong Joint Research Centre for Optical Fibre Sensors, Shenzhen University, Shenzhen 518060, China*
[*]*yingwang@szu.edu.cn*

Abstract: A new refractometer based on a fiber Mach–Zehnder interferometer incorporating an H-shaped optical fiber is proposed and demonstrated, which was fabricated by splicing a section of polarization-maintaining fiber between two sections of single-mode fibers and subsequent chemical corrosion. Real-time monitoring of the corrosion process during device manufacturing ensures a superior contrast ratio of interference fringes. The spectral characteristics of interferometers of different lengths and the refractive index sensing performance of interferometers were investigated experimentally. When the refractive index of the analyte is close to that of the fiber material, the proposed interferometer is still usable and exhibits an ultra-high sensitivity of 105502.51 nm/RIU. Furthermore, the availability and cost of the proposed interferometer are favorable as the expensive and sophisticated equipment is not required in the manufacturing process, and parallel processing is allowed. Such a simple fiber device can potentially be employed in high-accuracy biochemical detection.

© 2025 Optica Publishing Group under the terms of the Optica Open Access Publishing Agreement

1. Introduction

In recent years, biochemical detection technologies based on different optical principles (Raman spectroscopy, fluorescence imaging, etc.) have been widely applied in fields such as food detection, chemical analysis, medical diagnosis, and environmental control. Among these optical biochemical detection technologies, refractive index (RI) sensing technology is a relatively conventional and fast method. The numerical value of RI usually represents of the amount of a substance in the environment. Examine the subtle RI inconsistencies caused by differences in biochemical substance concentrations can achieve in-situ detection of analytes. Therefore, developing ultra-high sensitivity RI sensors is an effective way to achieve the detection and analysis of trace biochemical substances. Nowadays, there are many optical based RI detection instruments, such as the well-known Abbe refractometer [1] and surface plasmon resonance refractometer [2,3]. However, traditional optical RI detection instruments typically consist of numerous and bulky optical and mechanical components, with high cost, large volume, high analyte usage, and relatively poor stability limiting the detection applications of these refractometers in some biochemical fields.

Fiber optic RI sensors have attracted the attention of researchers due to their advantages such as simple structure, small size, remote online monitoring, easy multiplex, and networking. The

#567618 https://doi.org/10.1364/OE.567618
Journal © 2025 Received 12 May 2025; revised 24 Sep 2025; accepted 30 Sep 2025; published 13 Oct 2025

Optics EXPRESS

development of fiber optic refractometers is expected to fill some of the performance deficiencies of traditional refractometers in actual testing processes. The refractometers based on fiber Fresnel reflection can detect analytes by identifying the intensity change of the reflected signal [4]. This kind of sensor has the characteristics of easy manufacture, good resolution and high mechanical strength [5], and is widely used in the field of temperature sensing or RI analysis [6–8]. However, when used for a long time, the reflected signal seems to be more easily disturbed by the end surface cleanliness or light source fluctuation. Many optical fiber structures are also used for RI sensing or biochemical substances detection. These include U-shaped fibers [9,10], waist-deformed fiber taper [11], photonic crystal fibers [12], interferometers [13–15], surface plasmon resonance (SPR) [16,17], fiber microfluidic channels [18,19], long period fiber gratings (LPFG) [20,21], and tilted fiber gratings [22,23]. Among them, the fiber refractometer based on Mach-Zehnder interferometer (MZI) exhibits compact size and surprising sensitivity. However, relying on laser precision machining to manufacture MZIs is inefficient and costly [24,25]. MZIs based on twin-core hollow optical fibers may only be suitable for detecting analytes with RI lower than fiber materials [26].

Here, we propose a new optical fiber MZI based refractometer that combines low cost, compactness, and simplicity. This type of MZI can be obtained through ordinary fiber fusion splicing and subsequent chemical corrosion. The wide range and high sensitivity characteristics of this MZI refractometer have also been demonstrated. The proposed chemical corrosion technology allows for simultaneous processing of multiple samples, making it possible to achieve large-scale production of this optical fiber refractometer.

2. Principle and sensor fabrication

The RI sensor proposed in this article is based on a H-shaped optical fiber MZI structure. The novel MZI structure is shown schematically in Fig. 1 and consists of a conventional single-mode fiber (SMF) in which a short section of H-shaped optical fiber is inserted. As depicted in Fig. 1(a), an incident beam is first guided by the core of the lead-in SMF (i.e., SMF_{in}), and after transmission through the H-shaped optical fiber, it is finally coupled into the core of the lead-out SMF (i.e., SMF_{out}). Figure 1(b) and (c) are schematic diagrams of the cross-sections of SMF and H-shaped optical fiber, respectively. The enlarged diagram of the core area is shown in Fig. 1(d). Owing to the core cross-sectional shape mismatch, the light transmitted in the core of SMF_{in} is divided into two parts at the first splice joint. Part of the light is coupled into the core of the H-shaped optical fiber, while the other part is coupled into the external medium (Usually air or solution) around the H-shaped optical fiber core and transmitted forward through spatial light propagation. These two parts of light will be coupled together into the core of the SMF_{out} at the second splice joint. The existence of optical path difference between two optical paths will excite the well-known Mach-Zehnder interference in the core of the SMF_{out}, and the interference fringe patterns can be observed in the transmission spectra. Due to the correlation between the RI of the external medium or the optical path difference and the interference fringes [27,28], this MZI has the potential to become a sensor for environmental protection, food industry, or reagent concentration detection (e.g., detecting the concentration of glucose in an aqueous solution), and the H-shaped optical fiber works as the sensing region.

The intensity of light transmitted in the external medium and the H-shaped optical fiber core is denoted as I_1 and I_2, respectively. According to the theory of interference, the contrast of the fringes in the interference pattern strongly depends on the ratio of I_1 and I_2. Therefore, by adjusting the corrosion time to control the cross-sectional area of the H-shaped optical fiber core, the ratio of I_1 and I_2 can be optimized, thereby significantly improving the contrast of the interference fringe pattern.

The production of the proposed H-shaped optical fiber MZI structure mainly includes two processes: fiber fusion and hydrofluoric acid corrosion. The detailed preparation steps are

Optics EXPRESS

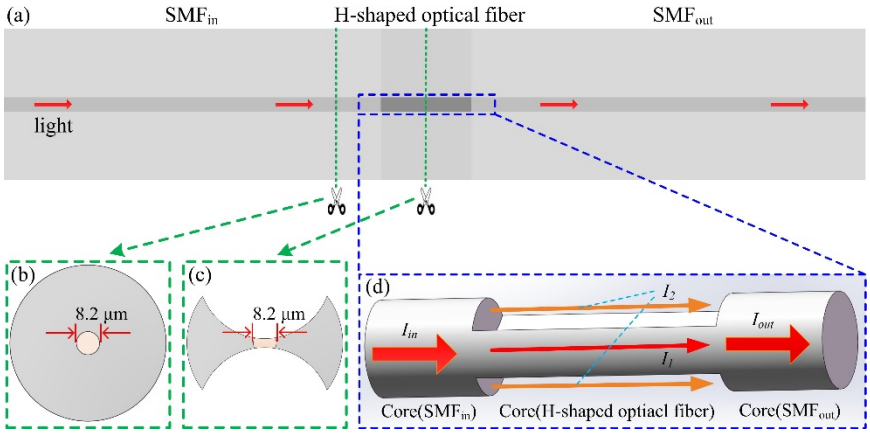

Fig. 1. Schematic diagram of the proposed MZI sensor. (a) The MZI sensor is formed by the H-shaped optical fiber between the two SMFs; (b) Geometric structure of SMF cross-section; (c) Geometric structure of H-shaped optical fiber cross-section; (d) Localized magnified view of the core region used to excite MZ interference.

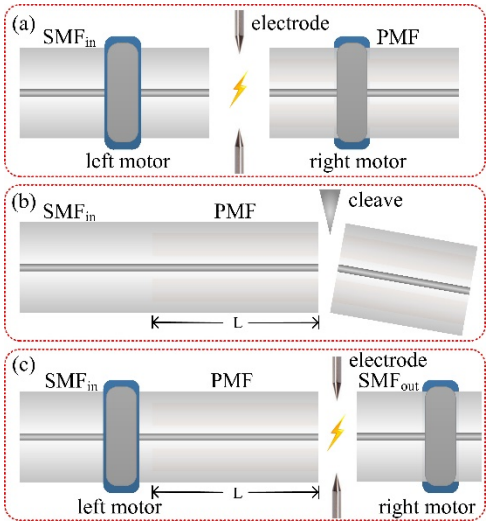

Fig. 2. Schematic diagram of device manufacturing process: (a) Splicing SMF$_{in}$ with PMF; (b) The PMF was cut to an exact length (L); (c) Splicing PMF with SMF$_{out}$.

shown in Fig. 2 and Fig. 3. Figure 2 provides a detailed explanation of the fiber fusion splicing steps in the device manufacturing process. Step one: a piece of polarization maintaining fiber (PMF, PM1550_125-13/250, YOFC, Wuhan, China) and a section of conventional SMF was spliced together by use of a fusion splicer (FSM-62S, Fujikura, Japan), and the splicing program parameter used has been optimized. In the second step, the PMF is accurately cleaved with a length L, as illustrated in Fig. 2(b). It's important to note that this cutting process requires the use of an optical amplification system to ensure the cutting accuracy. The third step, the end of PMF is connected to another standard SMF (i.e., SMF $_{out}$) by using the same arc discharge fusion parameter as mentioned above.

After splicing was completed, place this SMF-PMF-SMF structure into a polytetrafluoroethylene trough containing hydrofluoric acid for corrosion treatment. To ensure the homogenization

Optics EXPRESS

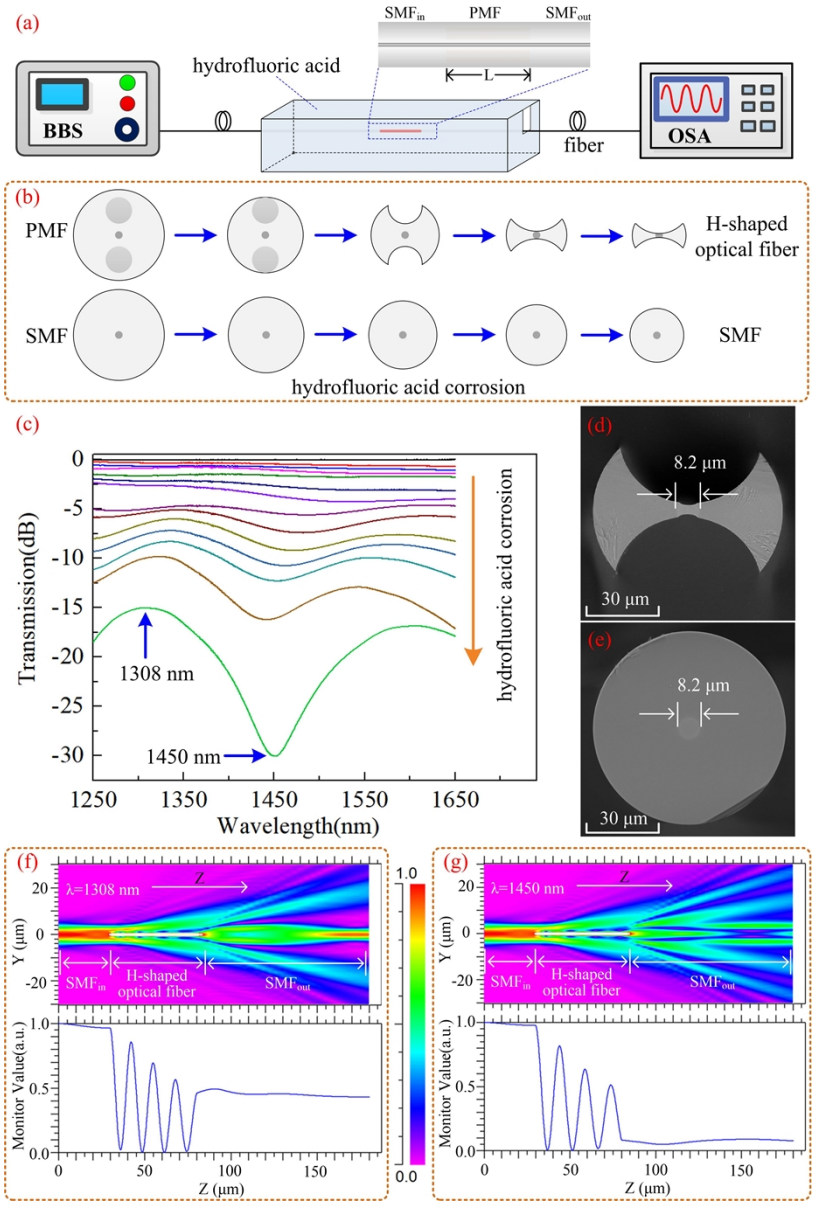

Fig. 3. (a) Schematic diagram of experimental system for real-time monitoring of corrosion progression; (b) Evolution of cross-section of PMF and SMF during chemical corrosion process; (c) Evolution of transmission spectra during corrosion process; (d) and (e) Scanning electron microscopy images of the H-shaped optical fiber and SMF cross-section; (f) and (g) Beam propagation simulation in the MZI at the wavelength of 1308 nm and 1450 nm, respectively.

of corrosion, the optical fiber should be fixed to ensure that it remains straight and suspended during the subsequent corrosion process, and the PMF should be placed in the middle position of the trough, while sufficient hydrofluoric acid is added to ensure that the fiber is completely submerged in the liquid. Due to the complete encapsulation of the fiber by hydrofluoric acid,

Optics EXPRESS

the chemical corrosion reaction will start from the cladding of the fiber and gradually develop towards the center of the fiber.

In order to accurately control the corrosion progress of optical fibers, the experimental setup shown in Fig. 3(a) was used to measure the spectra of the devices in real-time. The light emitted by a broadband light source (BBS, FL-ASE, Fiber Lake, Shenzhen, China) is incident into the SMF_{in}, while the signal output by the SMF_{out} is received and processed by an optical spectrum analyzer (OSA, AQ6370C, Yokogama, Tokyo, Japan). The purity of silica materials is usually a key factor in the corrosion rate. For PMF, the corrosion rate of highly doped stress zones by hydrofluoric acid is much higher than that of other areas. The cross-sectional morphology changes of SMF and PMF during the corrosion process are illustrated in Fig. 3(b). As the corrosion time increases, the PMF initially only decreases in the cladding diameter. When corrosion affects the high doping region of the PMF, this zone will be quickly eliminated, and the fiber cross-section will become H-shaped. As corrosion continues, a portion of the fiber core will be eliminated. Correspondingly, the cladding diameter of SMF gradually decreases due to the uniform elimination of its outer surface by hydrofluoric acid. After corrosion, the fiber is still considered a type of SMF due to its remaining cladding diameter still being much larger than the core diameter.

Figure 3(c) shows the transmission spectra evolution of the device during the corrosion process. When a small segment of PMF with a length of L is inserted between SMFs, the transmission spectrum of the device is shown by the black solid line in Fig. 3(c), indicating that the insertion loss can be ignored. The almost zero insertion loss of the SMF-PMF-SMF structure is mainly attributed to the fact that the PMF and SMF used in the experiment have the same core diameter and their mode fields have a good match. When the cladding thickness around the PMF core is sufficient, light can be well confined within the core, resulting in almost invisible loss in the transmission spectra. In order to quickly remove the fiber cladding, the initial concentration of hydrofluoric acid added to the trough is 40%. When an increase in loss is observed in the spectrum, the concentration of hydrofluoric acid is changed to 20% to reduce the corrosion rate, making it easier for us to control the corrosion progress by observing the evolution of the device's transmission spectra. The increase in loss is mainly due to insufficient thickness of the fiber cladding after corrosion, and even a part of the fiber core being corroded, as shown in Fig. 3(b). Therefore, the light in the fiber core will be leaked into the external medium. In Fig. 3(c), it can be seen that the earlier transmission spectrum curves have lower losses and no interference pattern can be observed. At this time, the PMF core should not have been corroded, but the surrounding cladding may have a very small thickness. Subsequently, the loss further increases while the visibility of interference fringes increases, indicating that the PMF core is beginning to suffer from corrosion and its cross-sectional area gradually decreases, which will result in a decrease in I_1 and an increase in I_2. When the interference fringe pattern in the spectrum reaches a satisfactory extinction ratio, it indicates that I_1 and I_2 are close to equal. At this point, hydrofluoric acid is sucked out of the trough and the fiber is cleaned with deionized water. After cleaning, the fiber is removed from the trough and dried.

Figure 3(d) displays the cross-sectional scanning electron microscope image of the H-shaped optical fiber obtained by etching the PMF with hydrofluoric acid, which shows the fiber core has been partially eliminated. Figure 3(e) shows an electron microscope image of a SMF cross-section on the obtained SMF-H-shaped optical fiber-SMF structure, it indicates that the SMF has an intact fiber core with a diameter of 8.2 μm (The cladding diameter of the SMF is less than 125 μm due to hydrofluoric acid corrosion processing). A full-vectorial beam propagation simulation results with different wavelength are shown in Fig. 3(f) and Fig. 3(g), where the beam propagation direction is z-axis. The results show that the light of SMF_{in} enters the H-shaped optical fiber and splits, then combines in the SMF_{out} core and finally forms interference. As

Optics EXPRESS

shown in Fig. 3(f) and Fig. 3(g), the power reaches the maximum point at the wavelength of 1308 nm and the minimum point at the wavelength of 1450 nm.

3. Results and discussions

The correlation between the length of H-shaped optical fibers and the transmission spectral characteristics of MZIs was investigated. Using the preparation method described above, three MZIs with different lengths (L = 50, 75, and 100 μm, respectively) of H-shaped optical fibers were fabricated in the experiment. These MZIs were immersed in deionized water, and the measured transmission spectra are shown in Fig. 4. Due to the real-time measurement of the transmission spectra and the accurate adjustment of the corrosion degree in the preparation process, the two arms of the interferometers can achieve a relatively uniform light energy distribution, which ensures the good fringe visibility of the interferometers and is conducive to improving the detection limit of the sensors. However, an increase in the length of the H-shaped optical fiber will lead to more light being leaked into the external medium. As shown in Fig. 4, the insertion loss of the three MZIs gradually increases with the increase in H-shaped optical fiber length. In addition, according to the well-known Mach-Zehnder interference theory, the free spectral range (FSR) of the interference fringe pattern is inversely proportional to the length of the interference arm. In this work, the length of the interference arm is equivalent to the length of the H-shaped optical fiber. when the H-shaped optical fiber length is 50 μm, only one interference dip (1452.68 nm) can be observed in the transmission spectrum and the FSR is significantly greater than the latter two. When the length of the H-shaped optical fiber increases to 75 μm and 100 μm, the FSR decreases to 213.82 nm and 144.51 nm, respectively.

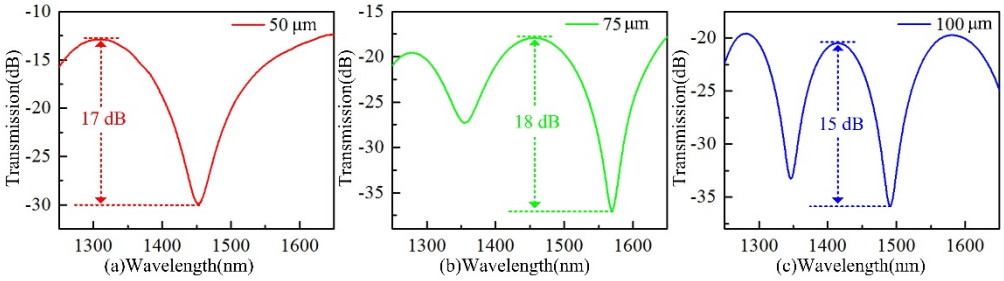

Fig. 4. Transmission spectra of three MZIs with different H-shaped optical fiber lengths. (a) 50 μm; (b) 75 μm; and (c) 100 μm.

To characterize the sensing performance of the proposed MZIs, the experimental setup shown in Fig. 5 was used to test the RI sensitivity of the sensor in different RI ranges. Seal an MZI into a capillary tube with an inner diameter of approximately 400 μm, which contains a commercial RI matching liquid (Cargille Lab, http://www.cargille.com) and its two ends are both sealed with glue to block liquid leakage. After packaging, the device is placed in a tube furnace, which has a resolution of 0.1 °C and a temperature adjustment range from room temperature to 100 °C. During the testing process, the RI of the liquid inside the capillary tube is precisely adjusted by setting different temperatures inside the tube furnace to explore the transmission spectral response of MZIs under different temperatures or external liquid RIs. It should be noted that spectral collection is carried out 15 minutes after the temperature setting is completed, ensuring that the furnace environment reaches a stable state.

The MZI sealed into the capillary tube in the experiment has an H-shaped optical fiber with a length of 100 μm, and the RI values of the RI matching liquids used are 1.33, 1.37, and 1.41 (589.3 nm, 25 °C), respectively. When the temperature inside the tube furnace increases from 25 °C to 35 °C in a step of 2 °C, as shown in Fig. 6(a)-(c), the interference fringes in the

Optics EXPRESS

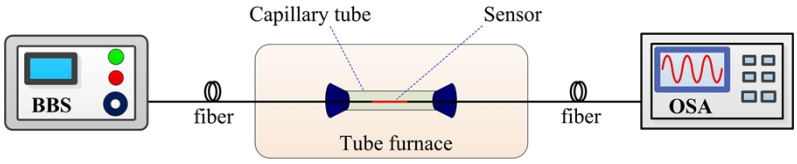

Fig. 5. Experimental apparatus for temperature/RI sensing testing.

transmission spectra of the device undergo a red shift. For interference fringe dips near 1400 nm, Fig. 6(a_1)-(c_1) shows the evolution of their wavelengths with increasing temperature, with sensitivities of 3.95, 4.95, and 8.83 nm/°C, respectively. In fact, the thermal optical coefficient of quartz materials is usually approaching two orders of magnitude smaller than that of liquids, so temperature induced changes in the RI of optical fiber materials can be ignored [29]. And the response of transmission spectra to temperature can be considered as its response to the change in RI of the liquid around the optical fiber caused by temperature increase [30] . The thermal optical coefficients of the RI matching liquids (1.33, 1.37, and 1.41) used in the experiment are -3.37 × 10^{-4}/°C, -3.42 × 10^{-4}/°C, and -4.08 × 10^{-4}/°C, respectively. Therefore, based on the calculated temperature sensitivity above, the RI sensitivity of the device to the liquid around the fiber are -11721.07, -14473.68, and -21642.16 nm/RIU, respectively, indicating that the proposed MZI sensors have satisfactory detection sensitivity in these RI ranges. As we know, when the mth order interference fringe dip wavelength is λ_m and the difference between the RI of the analyte and the effective RI of the fiber core is Δn, the sensitivity of the MZI can be expressed as [27]: $S = d\lambda_m/d(\Delta n) = \lambda_m/\Delta n$. So, the experimental results are consistent with the theory, that is, the sensitivity will increase as the RI difference decreases. For the above three tested RIs (1.33,1.37, and 1.41), the full-width-half-maximum (FWHM) of the interference dips is 55, 80 and 117 nm respectively. If the signal-to-noise ratio (SNR) is 50 dB, the detection limits of the sensor in these RI ranges can be calculated according to the known sensitivity [31], which are 1.76 × 10^{-4}, 2.07 × 10^{-4}, and 2.03 × 10^{-4} RIU, respectively.

Actually, in the process of detecting biochemical substances, the RI difference between many chemical reagents or solutions to be analyzed and optical fiber core is relatively small (For example, many benzene derivatives have RI values around 1.49, and the effective RI of the fiber core [32] is close to this value), in this case, if the output wavelength range of the light source or the detection bandwidth of the OSA is limited, it is necessary to reduce FSR by increasing the length of the interference arm to ensure that interference fringe dip can be observed in the transmission spectra of the MZI sensor and sensing detection can be carried out. Unfortunately, when using femtosecond laser reducing material manufacturing methods to produce fiber MZI, the processing time will increase linearly with the length of the interference arm or microcavity. For the MZI manufactured using the chemical etching method proposed in this article, an increase in the longitudinal length of the H-shaped optical fiber (i.e., the length of the interference arm) will not affect the processing time, making it easy to manufacture MZI with an interference arm length of several hundred micrometers. A MZI with an H-shaped optical fiber length of 470 μm was fabricated in the experiment and its sensing characteristics were investigated using a standard RI matching liquid of 1.49, the thermal optical coefficient of this RI matching liquid is -3.98 × 10^{-4}/°C. Still using the experimental setup shown in Fig. 5 for testing, this MZI was immersed in a 1.49 RI matching liquid and the packaged device was placed into the tube furnace. Raise the temperature from 25 °C to 30 °C with a heating step of 1 °C, and the spectra of the MZI at different temperatures are shown in Fig. 7(a). As the temperature increases (i.e., the RI value of the RI matching liquid decreases), the interference fringe dip of the MZI moves regularly towards the shortwave direction. This result is exactly opposite to the test results above, because the RI of the liquid used here is greater than that of the optical fiber material, and an

Optics EXPRESS

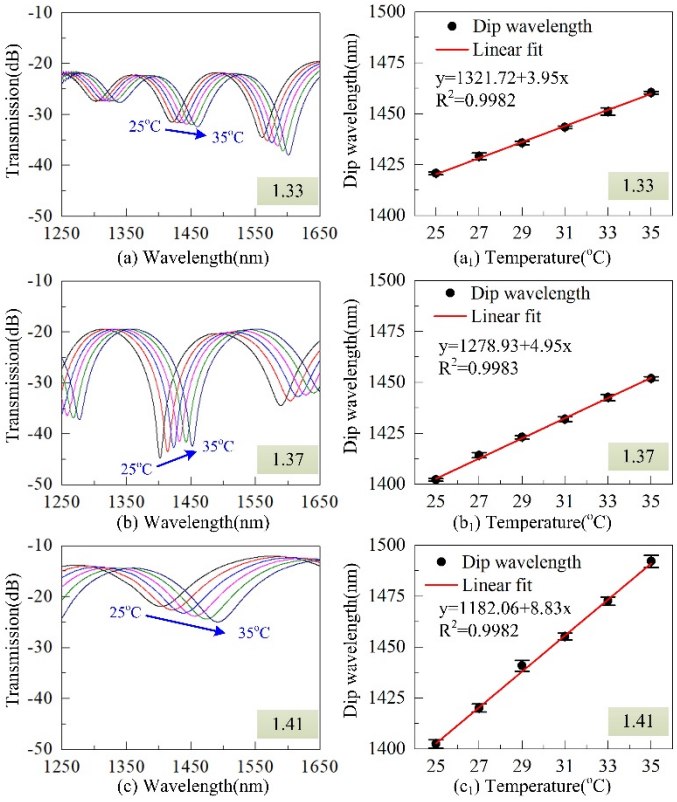

Fig. 6. Transmission spectra of RI matching liquid sealed MZIs at different temperatures: (a) The RI of the liquid is 1.33; (b) The RI of the liquid is 1.37; (c) The RI of the liquid is 1.41. (a_1-c_1) The variation of interference fringe dip wavelength with temperature when MZIs are sealed with different RI matching liquids (1.33, 1.37, and 1.41).

increase in temperature will reduce the RI difference between the two arms of the interferometer. Figure 7(b) shows the variation of interference fringe dip wavelength with temperature values, the MZI sensor exhibits satisfactory linear response ($R^2 = 0.9996$) to temperature and achieves high sensitivity of -41.99 nm/°C in the temperature range of 25 to 30 °C. Based on the known thermal optical coefficient of the 1.49 RI matching liquid, the RI sensitivity of MZI sensors can be calculated to be 105502.51 nm/RIU. In addition, the FWHM of the interference dip here is 145 nm, and the lower detection limit can be obtained as 5.15×10^{-5} RIU by using the similar calculation method mentioned above, indicating the sensor has promising application prospects in the field of biochemical sensing.

In order to demonstrate that the proposed fiber MZI RI sensor can be mass-produced through chemical etching methods, we placed multiple samples in parallel in a polytetrafluoroethylene trough and added hydrofluoric acid to synchronously corrode these samples. Subsequently, the spectra of five MZIs (named S_1-S_5) obtained from a single corrosion operation were measured experimentally, and the sensitivity of these MZIs for glucose concentration detection was examined. Figure 8(a) shows the spectra of five MZIs with a H-shaped optical fiber length of 100 µm in deionized water (i.e., glucose concentration is 0 mg/ml). It can be seen that the interference fringe dip wavelengths of the five MZIs obtained by a single corrosion have slight differences, mainly due to the unavoidable subtle differences in H-shaped optical fiber length (i.e., interference arm length) caused by fiber cutting errors. When the concentration

Optics EXPRESS

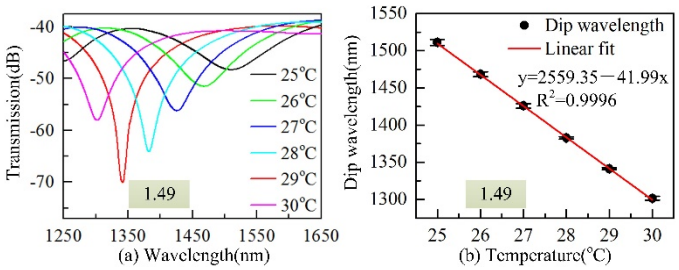

Fig. 7. Evolution of (a) transmission spectral profile and (b) interference fringe dip wavelength with temperature values when MZI (the length of MZI's H-shaped optical fiber is 470 μm) is immersed in a 1.49 RI matching liquid.

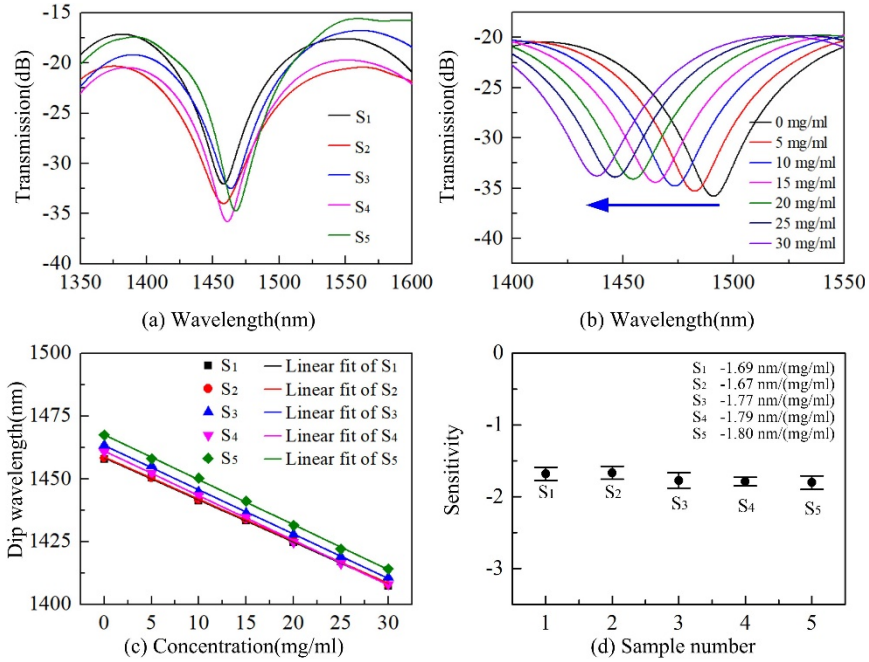

Fig. 8. (a) Transmission spectra of five MZIs (immersed in deionized water) obtained from a single corrosion operation; (b) Transmission spectral evolution of one MZI to varying concentrations of glucose solution; (c) Plot of dip wavelength against concentrations of glucose solution; (d) The sensitivity obtained by these five MZIs.

of glucose solution around these interferometers increases, the interference fringes dips shift towards shorter wavelengths, and the transmission spectral evolution of one of the interferometers is shown in Fig. 8(b). Figure 8(c) shows the correspondence between the dip wavelengths of these interferometers and glucose concentration. To verify the long-term stability of the sensors, repeated tests were conducted on each interferometer, and the average and standard deviation of sensitivity are shown in Fig. 8(d). The sensitivity obtained is about forty times higher than previously reported [33], and there are slight differences in the sensitivity of each MZI, as shown in Fig. 8(d). The final average sensitivity of these five MZIs obtained was -1.74 nm/(mg/ml), with a maximum sensitivity error of only 4.02%, indicating that these MZIs have good sensitivity consistency when used for sensing.

Optics EXPRESS

We measured the RI of glucose aqueous solutions with different concentrations using a digital Abbe refractometer and performed linear fitting. The results show that the RI of glucose solution can be expressed as: $n = 1.3356 \pm 1.4571 \times 10^{-4}$C, where C refers to the concentration of glucose aqueous solution. In our experiment, the concentration of glucose aqueous solution increased from 0 to 30 mg/ml, and the RI range was 1.3356-1.3400. Therefore, we can calculate that the sensitivity of the sensor within this RI range was 11941.52 nm/RIU, which was similar to that in literature [27]. Table 1 shows the sensing performance of previously reported optical fiber RI sensors. Compared with other types of RI sensors, the H-shaped optical fiber MZI sensor proposed in this work has comparable or higher sensitivity.

Table 1. Comparison of the optical fiber RI sensors' performance

Structure	Range	Sensitivity	Reference
hole-assisted dual-core fiber	1.335-1.395	353.9 nm/RIU	[15]
laser inscribed MZI	~1.432	~3000 nm/RIU	[24]
MZI created in twin-core fiber	1.30-1.34	10981 nm/RIU	[27]
Sagnac interferometer	1.3322-1.3371	2849 nm/RIU	[34]
SPR sensor	1.332-1.336	22248 nm/RIU	[17]
Hollow-core fiber	1.33-1.34	1064.6 nm/RIU	[19]
Functionalized LPFG	1.333-1.347	2538 nm/RIU	[21]
MZI in H-shaped fiber	~1.33	11721.07 nm/RIU	this work

4. Conclusions

Summarizing, this article demonstrates a novel MZI formed by an SMF-H-shaped optical fiber-SMF structure, and the manufacturing process of the interferometer only includes conventional fiber fusion and subsequent chemical corrosion. By monitoring the transmission spectra of the device in real-time during the corrosion process, PMF can be easily processed into H-shaped optical fiber with controllable core cross-sectional area to manufacture fiber MZI with high visibility of interference fringes. The research on the sensing characteristics of fiber MZI for RI shows that the proposed MZI sensor has a significant wavelength response to tiny changes in the RI of external liquids, despite the fact that external liquids have different initial RIs. In addition, relying on the high tolerance of chemical corrosion processing technology for the longitudinal processing length of optical fibers, a MZI sensor with interference arm's length of 470 µm was easily prepared, and its RI sensitivity reached up to 105502.51 nm/RIU when the liquid RI was around 1.49. In the actual biomedical or chemical application scenarios, multiplexing may be required. The low-cost sensing structure can realize the simultaneous detection of several analytes with the help of multi-channel optical fiber sensor demodulator. Based on its demonstrated advantages, such as simple structure and low-cost manufacturing process, the proposed high-sensitivity RI sensor is expected to be applied in the fields such as biochemical substance analysis or environmental monitoring.

Funding. National Natural Science Foundation of China (62475170, 62122057); Natural Science Foundation of Guangdong Province (2023A1515012893, 2022B1515120061); Shenzhen Science and Technology Innovation Program (JCYJ20220818095615034, ZDSYS20220606100405013).

Disclosures. The authors declare no conflicts of interest.

Data availability. Data underlying the results presented in this paper are not publicly available at this time but may be obtained from the authors upon reasonable request.

References

1. J. Rheims, J. Koser, and T. Wriedt, "Refractive-index measurements in the near-IR using an Abbe refractometer," Meas. Sci. Technol. **8**(6), 601–605 (1997).

Optics EXPRESS

2. H. M. Liang, H. Miranto, N. Granqvist, *et al.*, "Surface plasmon resonance instrument as a refractometer for liquids and ultrathin films," Sens. Actuators, B **149**(1), 212–220 (2010).
3. Y. J. Zeng, J. Zhou, X. L. Wang, *et al.*, "Wavelength-scanning surface plasmon resonance microscopy: A novel tool for real time sensing of cell-substrate interactions," Biosens. Bioelectron. **145**, 111717 (2019).
4. C. L. Zhao, J. H. Li, S. Q. Zhang, *et al.*, "Simple Fresnel Reflection-Based Optical Fiber Sensor for Multipoint Refractive Index Measurement Using an AWG," IEEE Photonics Technol. Lett. **25**(6), 606–608 (2013).
5. J. H. Chen, X. G. Huang, W. X. He, *et al.*, "A parallel-multipoint fiber-optic temperature sensor based on Fresnel reflection," Opt. Laser Technol. **43**(8), 1424–1427 (2011).
6. M. G. Shlyagin, R. M. Manuel, and O. Esteban, "Optical-fiber self-referred refractometer based on Fresnel reflection at the fiber tip," Sens. Actuators, B **178**, 263–269 (2013).
7. A. Brientin, D. Leduc, V. Gaillard, *et al.*, "Numerical and experimental study of a multimode optical fiber sensor based on Fresnel reflection at the fiber tip for refractive index measurement," Opt. Laser Technol. **143**, 107315 (2021).
8. R. Martínez-Manuel, O. Esteban, and M. G. Shlyaginc, "Simple low-cost refractometer using a disposable optical fiber tip for measurements," Opt. Eng. **55**(11), 116108 (2016).
9. R. Bharadwaj, V. V. R. Sai, K. Thakare, *et al.*, "Evanescent wave absorbance based fiber optic biosensor for label-free detection of E. coli at 280 nm wavelength," Biosens. Bioelectron. **26**(7), 3367–3370 (2011).
10. J. Dong, M. Sang, S. Wang, *et al.*, "Ultrasensitive Label-Free Biosensor Based on the Graphene-Oxide-Coated-U-Bent Long-Period Fiber Grating Inscribed in a Two-Mode Fiber," J. Lightwave Technol. **39**(12), 4013–4019 (2021).
11. M. Sypabekova, S. Korganbayev, W. Blanc, *et al.*, "Fiber optic refractive index sensors through spectral detection of Rayleigh backscattering in a chemically etched MgO-based nanoparticle-doped fiber," Opt. Lett. **43**(24), 5945–5948 (2018).
12. T. S. Li, L. Q. Zhu, X. C. Yang, *et al.*, "A Refractive Index Sensor Based on H-Shaped Photonic Crystal Fibers Coated with Ag-Graphene Layers," Sensors **20**(1), 10 (2019).
13. Z. Jiangtao, W. Yiping, L. Changrui, *et al.*, "Intensity modulated refractive index sensor based on optical fiber Michelson interferometer," Sens. Actuators, B **208**, 315–319 (2015).
14. B. Xu, Y. Yang, Z. Jia, *et al.*, "Hybrid Fabry-Perot interferometer for simultaneous liquid refractive index and temperature measurement," Opt. Express **25**(13), 14483–14493 (2017).
15. J. Yang, M. Yang, C. Y. Guan, *et al.*, "In-fiber Mach-Zehnder interferometer with piecewise interference spectrum based on hole-assisted dual-core fiber for refractive index sensing," Opt. Express **26**(15), 19091–19099 (2018).
16. Y. E. Monfared, "Refractive Index Sensor Based on Surface Plasmon Resonance Excitation in a D-Shaped Photonic Crystal Fiber Coated by Titanium Nitride," Plasmonics (2019).
17. B. Wang, Y. Niu, S. Zheng, *et al.*, "An Optical Fiber Immunosensor With a Low Detection Limit Based on Plasmon Coupling Enhancement," J. Lightwave Technol. **38**(14), 3781–3788 (2020).
18. J. Yang, C. Guan, P. Tian, *et al.*, "In-fiber refractive index sensor based on single eccentric hole-assisted dual-core fiber," Opt. Lett. **42**(21), 4470–4473 (2017).
19. Y. Wang, R. Gao, and X. Xin, "Hollow-core fiber refractive index sensor with high sensitivity and large dynamic range based on a multiple mode transmission mechanism," Opt. Express **29**(13), 19703–19714 (2021).
20. L. Rindorf and O. Bang, "Highly sensitive refractometer with a photonic-crystal-fiber long-period grating," Opt. Lett. **33**(6), 563–565 (2008).
21. C. Liu, Q. Cai, B. J. Xu, *et al.*, "Graphene oxide functionalized long period grating for ultrasensitive label-free immunosensing," Biosens. Bioelectron. **94**, 200–206 (2017).
22. B. Q. Jiang, K. M. Zhou, C. L. Wang, *et al.*, "Label-free glucose biosensor based on enzymatic graphene oxide-functionalized tilted fiber grating," Sens. Actuators, B **254**, 1033–1039 (2018).
23. T. Guo, F. Liu, X. Liang, *et al.*, "Highly sensitive detection of urinary protein variations using tilted fiber grating sensors with plasmonic nanocoatings," Biosens. Bioelectron. **78**, 221–228 (2016).
24. Y. Zhang, C. Lin, C. Liao, *et al.*, "Femtosecond laser-inscribed fiber interface Mach-Zehnder interferometer for temperature-insensitive refractive index measurement," Opt. Lett. **43**(18), 4421–4424 (2018).
25. M. Janik, S. V. Hamidi, M. Koba, *et al.*, "Real-time isothermal DNA amplification monitoring in picoliter volumes using an optical fiber sensor," Lab Chip **21**(2), 397–404 (2021).
26. X. Yang, W. Yu, Z. Liu, *et al.*, "Optofluidic twin-core hollow fiber interferometer for label-free sensing of the streptavidin-biotin binding," Sens. Actuators, B **277**, 353–359 (2018).
27. Z. Li, C. Liao, Y. Wang, *et al.*, "Ultrasensitive refractive index sensor based on a Mach-Zehnder interferometer created in twin-core fiber," Opt. Lett. **39**(17), 4982–4985 (2014).
28. T. Zhu, Z. Ou, M. Han, *et al.*, "Propylene Carbonate Based Compact Fiber Mach-Zehnder Interferometric Electric Field Sensor," J. Lightwave Technol. **31**(10), 1566–1572 (2013).
29. D. K. C. Wu, B. T. Kuhlmey, and B. J. Eggleton, "Ultrasensitive photonic crystal fiber refractive index sensor," Opt. Lett. **34**(3), 322–324 (2009).
30. T. Han, Y. G. Liu, Z. Wang, *et al.*, "Unique characteristics of a selective-filling photonic crystal fiber Sagnac interferometer and its application as high sensitivity sensor," Opt. Express **21**(1), 122–128 (2013).
31. I. M. White and X. Fan, "On the performance quantification of resonant refractive index sensors," Opt. Express **16**(2), 1020–1028 (2008).
32. F. Zhang, X. Xu, J. He, *et al.*, "Highly sensitive temperature sensor based on a polymer-infiltrated Mach-Zehnder interferometer created in graded index fiber," Opt. Lett. **44**(10), 2466–2469 (2019).

Optics EXPRESS

33. N. F. F. Areed, M. F. O. Hameed, and S. S. A. Obayya, "Highly sensitive face-shaped label-free photonic crystal refractometer for glucose concentration monitoring," Opt. Quantum Electron. **49**(1), 5 (2017).
34. N. Zhang, K. Li, Y. Cui, *et al.*, "Ultra-sensitive chemical and biological analysis via specialty fibers with built-in microstructured optofluidic channels," Lab Chip **18**(4), 655–661 (2018).